Rama, G.; Marinkovic, D.; Zehn, M.

Efficient three-node finite shell element for linear and geometrically nonlinear analyses of piezoelectric laminated structures

Rama, G., Marinković, D., & Zehn, M. (2017). Efficient three-node finite shell element for linear and geometrically nonlinear analyses of piezoelectric laminated structures. Journal of Intelligent Material Systems and Structures, 29(3), 345–357. https://doi.org/10.1177/1045389x17705538

Efficient 3-node finite shell element for linear and geometrically nonlinear analysis of piezoelectric laminated structures

Gil Rama, Dragan Marinković, Manfred Zehn

Department of Structural Analysis, Berlin Institute of Technology, Germany

Abstract

Fiber-reinforced composite laminates involving piezoelectric layers represent a very attractive material system. It combines the advantages of using rather lightweight and stiff material with the possibility of sensing structural changes and actively influencing its state by means of sensors and actuators. A 3-node shell element is proposed as an efficient tool for modeling structures made of such a material system. Thoroughly tested solutions are implemented to resolve locking problems intrinsic for shell elements. The embedded piezoelectric layers are considered to be polarized in the thickness direction. Furthermore, the extension of the formulation to geometrically nonlinear finite element (FE) analysis is based on a co-rotational formulation. Numerical examples are given to demonstrate the applicability of developed element in linear and geometrically nonlinear FE analysis covering both actuator and sensor cases.

Keywords: shell element, piezoelectricity, active laminates, co-rotational FEM, actuator, sensor

1 INTRODUCTION

Over the last two decades, active/smart structures have attracted substantial research attention. The essence of the idea relies on transforming a passive system into an active one by adding/embedding active elements, i.e. sensors and actuators. Connecting sensors with actuators

via a controller allows implementation of a control law with the aim of controlling the structural behavior according to a predefined strategy. For high-integration ability of active elements into the passive structure, actuators and sensors are often made of multifunctional materials, which beside the carrying capacity also feature coupling between the mechanical field and some other field. In the case of piezoelectric materials, the coupling is achieved between the mechanical and electric fields. Hence, one may directly influence the mechanical field through a purposeful control of the electric field – actuator case. Vice versa, information on the induced electric field in the piezoelectric-based component provides information on the induced deformation (i.e. strain field) – sensor case.

Fiber-reinforced composite laminates with bonded/embedded piezoelectric layers are among material systems of most practical interest in a variety of applications involving automotive, aerospace, aeronautical applications, to name but a few. Beside the exquisite properties of composites, the presence of active elements in such a material system offers a great potential for improved vibration and/or shape control, radiated noise reduction, etc. (Aridogan and Basdogan, 2015). These advantages render their design and analysis of their behavior even more challenging.

Whereas in the beginning of the ‘90s some analytical considerations of the problem were reported (Lee 1990; Dökmeci, 1990; Lee and Moon, 1990; Wang and Rogers 1991), the attention was turned later to the finite element method (FEM) as a predominant numerical method in the field of structural analysis. The FEM development in this particular field is prohibitively large for an exhaustive overview. The survey from Benjeddou (2000) provides a thorough overview of the development during the ‘90s. At the same time, Kioua and Mirza (2000) have provided solutions for a set of examples involving plain and shallow shell structures that have been resolved by means of the Ritz approach and based on the shallow shell assumptions. Those examples served as benchmark cases for a number of later FEM developments in the field. And the FEM developments proceeded at the same rapid pace in the decades to follow as this appears

to be a task that gives an ever-increasing impetus to the researchers to provide highly efficient and reliable tools to the engineers. The work, though focused to FE formulations for the considered type of structures, was still divergent in specific details. Some of the developments were focused on 3D elements. Lee et al. (2004) proposed a 3D piezoelectric solid element that can be used for modeling thin sensors and actuators whereby the assumed strain formulation was used as a remedy to avoid triggering transverse shear and membrane locking. Similarly, Klinkel and Wagner (2008) developed an 8-node piezoelectric solid shell element based on a mixed variational formulation that is applicable to linear and geometrically nonlinear formulation. Willberg and Gabbert (2012) used the isogeometric approach to develop a 3D piezoelectric finite element for smart structure applications.

A vast majority of developments were focused on finite elements that offer greater numerical efficiency in modeling thin-walled structures and aim at global structural behavior. Hence, shell type finite elements were addressed. A number of formulations based on the equivalent single-layer approach have been proposed for modeling laminated structures with piezolayers. Those elements mainly rely either on the Kirchhoff-Love or Mindlin-Reissner kinematics. Gabbert et al. (2002) extended the Semi-Loof element by Irons (1976) to an electro-mechanical coupled element, thus using the classical Kirchhoff-Love theory. However, the necessary C^1-continuity inherent in models based on this theory has always been one of the major obstacles for the development of efficient finite element formulations. In addition, the Mindlin-Reissner kinematics is also favored for laminated structures due to the greater impact of transverse shear effect in their behavior, which is covered by this theory. Zemčík et al. **(**2007**)** proposed a linear 4-node element with discrete shear gap (DSG) implemented to resolve shear locking effects intrinsic for linear element based on the Mindlin-Reissner kinematics. Marinkovic et al. **(**2006**)** developed a full-biquadratic 9-node degenerated shell element for modeling laminated fiber-reinforced structures with piezolayers. The element was further used to investigate the convergence of FEM results when modeling coupled piezoelectric problems (Marinković D and

Marinković Z, 2012) and, for the users' convenience, it was also implemented in the commercial FEA program ABAQUS (Nestorović et al., 2014). Kulikov and Plotnikova (2011) proposed piezoelectric 4-node shell element characterized by exact modeling of geometry, which was achieved using particular spline functions. Also with the aim of addressing the problem of accurate geometry description, Phung-Van et al. **(**2015**)** used the isogeometric approach in combination with a higher-order shear deformation theory to develop 2D elements for the analysis of composite laminates with piezoelectric sensors and actuators. For the sake of completeness, it should be mentioned that meshless approaches have also been addressed recently to model the considered type of structures (Stanak, 2015).

Layer-wise theories were also applied in modeling piezoelectric thin-walled structures. Ballhause et al. (2005) used both equivalent single-layer and layer-wise theories with linear and up to fourth-order expansions for the displacement variables. Cinefra et al. (2015a) performed linear static analyses with the developed a 9-node plate element based on mixed interpolation of tensorial components (MITC) approach and with variable through-the-thickness layer-wise kinematics. The developed element was also used for free-vibration analyses of plate structures with piezopatches (Cinefra et al, 2015b). Milazzo (2016) considered families of both equivalent single-layer and layer-wise elements for analysis of smart multilayered plates by applying the strategy that reduces the multi-field problem to an effective mechanical one by the condensation of electromechanical state into the plate kinematics.

Geometrically nonlinear problems of structures with integrated piezolayers have been treated considerably less in the literature. However, high slenderness combined with properties of modern composite laminates render these structures prone to moderate rotations, whereby the strains remain small. Such a behavior calls for geometrically nonlinear formulations. This has been recognized by some authors (Rabinovitch, 2005; Kulkarni and Bajoria, 2007; Lentzen et al., 2007).

In the present work, a highly efficient 3-node shell element for modeling of the considered type of structures is proposed. Consideration of the mechanical field relies on the development by Bletzinger et al. (2000) and Nguyen et al. (2013) and it has been extended here to cover geometrically nonlinear effects by means of the numerically efficient co-rotational approach (Chrisfield and Moita, 1996; Felippa and Haugen, 2005; Nguyen et al., 2015). Several sensor and actuator cases are presented to verify applicability of developed element and formulation by comparing the obtained results with solutions available in the literature.

2 FORMULATION OF THE ELEMENT

2.1 Coordinate systems and geometry of the element

The Discrete Shear Gap (DSG3) element was first developed by Bletzinger et al. (2000) and further improved by Nguyen et al. (2013) by implementing the strain smoothing technique. The improvements provided by Nguyen et al. (2013) are better accuracy and stability accompanied by the independence of element formulation from the node numbering sequence. The shell element formulation demands application of two coordinate systems to describe the element geometry, displacement and strain field as well as coupling between the mechanical and electric fields. Besides the global coordinate system (x, y, z), an element coordinate system (x′, y′, z′) is introduced (see Fig 1). The transformation matrix [T] between the global and local element coordinates reads:

$$[T] = \left[\{e_{x'}\} \quad \{e_{y'}\} \quad \{e_{z'}\} \right] \tag{1}$$

where the vectors $\{e_{x'}\},\{e_{y'}\},\{e_{z'}\}$ are defined so that the local x′-axis is oriented from node 1 toward node 2 and the z′-axis is perpendicular to the element surface (thickness direction):

$$\{e_{x'}\} = \frac{\{x_2 - x_1 \quad y_2 - y_1 \quad z_2 - z_1\}^T}{\left|\{x_2 - x_1 \quad y_2 - y_1 \quad z_2 - z_1\}^T\right|} \tag{2}$$

$$\{e_{31'}\} = \frac{\{x_3 - x_1 \quad y_3 - y_1 \quad z_3 - z_1\}^T}{\left|\{x_3 - x_1 \quad y_3 - y_1 \quad z_3 - z_1\}^T\right|} \tag{3}$$

$$\{e_{z'}\} = \{e_{x'}\} \times \{e_{31'}\} \tag{4}$$

$$\{e_{y'}\} = \{e_{z'}\} \times \{e_{x'}\} \tag{5}$$

with x_i, y_i and z_i denoting coordinates of the three nodes in the global coordinate system.

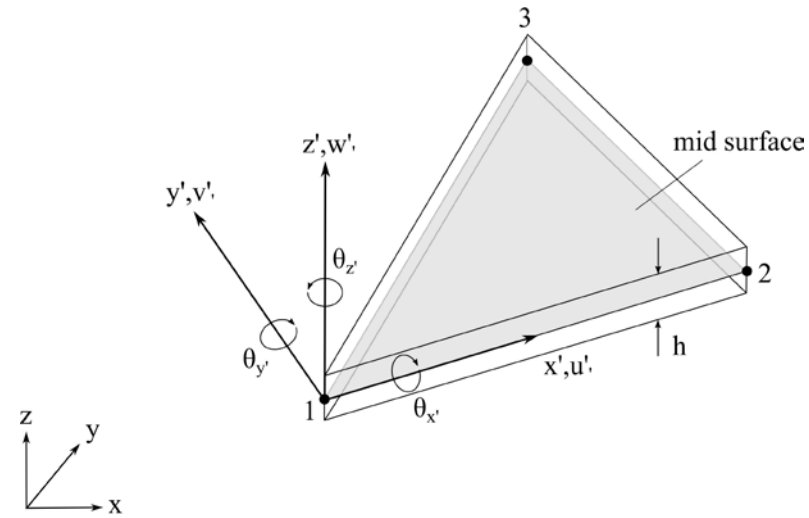

Fig. 1 Geometry and coordinate systems of the 3-node shell element

The shape functions are defined with respect to the element coordinates x′ and y′:

$$\begin{aligned}
N_1(x',y') &= \frac{1}{2A_e}[(x'_1 y'_3 - x'_3 y'_2) + (y'_2 - y'_3)x' + (x'_3 - x'_2)y'] \\
N_2(x',y') &= \frac{1}{2A_e}[(x'_3 y'_1 - x'_1 y'_3) + (y'_3 - y'_1)x' + (x'_1 - x'_3)y'] \\
N_3(x',y') &= \frac{1}{2A_e}[(x'_1 y'_2 - x'_2 y'_1) + (y'_1 - y'_2)x' + (x'_2 - x'_1)y']
\end{aligned} \tag{6}$$

where x'_i and y'_i, i=1, 2, 3, are the x′- and y′-coordinates of the three nodes in the element coordinate system and A_e is the element area. The shell thickness is considered to be in the normal direction to the mid-surface. Hence, the shell geometry with respect to the local coordinate system is easily generated using the mid-surface geometry and thickness direction:

$$\begin{Bmatrix} x' \\ y' \\ z' \end{Bmatrix} = \sum_{i=1}^{3} N_i \begin{Bmatrix} x'_i \\ y'_i \\ 0 \end{Bmatrix} + \sum_{i=1}^{3} \frac{h}{2} N_i t \{e_{z'}\} \tag{7}$$

with the shell thickness h, and -1<t<+1.

2.2 Element displacement and strain field

The element formulation implements the Mindlin-Reissner kinematical assumption, thus accounting for the transverse shear effects. The displacement of any point in the element domain is given with respect to the element coordinate system as a superposition of the corresponding mid-surface point displacements, u′, v′ and w′ along local directions x′, y′ and z′, respectively, and a linear function of the rotations about the local x′- and y′-axis through the same mid-surface point, $\theta_{x'}$ and $\theta_{y'}$. The required mid-surface point displacements and rotations are obtained using the nodal values (denoted by index i) and shape functions:

$$\begin{Bmatrix} u' \\ v' \\ w' \end{Bmatrix} = \sum_{i=1}^{3} N_i \begin{Bmatrix} u'_i \\ v'_i \\ w'_i \end{Bmatrix} + \sum_{i=1}^{3} \frac{h}{2} N_i t \begin{Bmatrix} \theta_{i,y'} \\ -\theta_{i,x'} \\ 0 \end{Bmatrix} \tag{8}$$

The strain field developed in the local element coordinate system has the following principle form:

$$\{\varepsilon'\} = \begin{Bmatrix} \{\varepsilon'_{mf}\} \\ -- \\ \{\varepsilon'_s\} \end{Bmatrix} = \begin{bmatrix} [B_{mf}] \\ -- \\ [B_s] \end{bmatrix} \{d'\} = [B_u] \begin{Bmatrix} \{d'_1\} \\ \{d'_2\} \\ \{d'_3\} \end{Bmatrix} \tag{9}$$

where $\{\varepsilon'_{mf}\}$ is the membrane-flexural (in-plane) strain field, $\{\varepsilon'_s\}$ are transverse shear strains, $[B_{mf}]$ and $[B_s]$ denote the corresponding strain-displacement matrices, respectively, and the vector $\{d_i'\}$ contains the nodal degrees of freedom – translations and rotations $\{d'_i\}=\{u'_i\ v'_i\ w'_i\ \theta_{i,x'}\ \theta_{i,y'}\}^T$. According to the DSG3 formulation (Nguyen et al., 2013) the nodal in-plane strain displacement nodal matrices are given as follow:

$$\left[B_{mf,i}\right]=\begin{bmatrix} N_{i,x'} & 0 & 0 & N_{i,x'} & 0 \\ 0 & N_{i,y'} & 0 & -N_{i,y'} & 0 \\ N_{i,y'} & N_{i,x'} & 0 & -N_{i,x'} & N_{i,y'} \end{bmatrix} \tag{10}$$

where, $N_{i,x'}$ and $N_{i,y'}$ (i = 1,2,3) are the constant derivatives of the shape functions in the local element coordinate system. As previously mentioned, the DSG3 element eliminates shear locking effects by utilizing the 'shear gap' concept (Bletzinger et al., 2000) along the element edges. The resulting nodal shear strain-displacement matrices become (Nguyen et al., 2013):

$$\begin{aligned} \left[B_{s,1}\right] &= \frac{1}{2A_e}\begin{bmatrix} 0 & 0 & b-c & 0 & -A_e \\ 0 & 0 & d-a & A_e & 0 \end{bmatrix} \\ \left[B_{s,2}\right] &= \frac{1}{2A_e}\begin{bmatrix} 0 & 0 & c & -bc/2 & ac/2 \\ 0 & 0 & -d & bd/2 & -ad/2 \end{bmatrix} \\ \left[B_{s,3}\right] &= \frac{1}{2A_e}\begin{bmatrix} 0 & 0 & -b & bc/2 & bd/2 \\ 0 & 0 & a & -ac/2 & ad/2 \end{bmatrix} \end{aligned} \tag{11}$$

with *a*, *b*, *c* and *d* denoting the following geometric dimensions:

$$\begin{aligned} a &= x'_2 - x'_1 \quad b = y'_2 - y'_1 \\ c &= y'_3 - y'_1 \quad d = x'_3 - x'_1 \end{aligned} \tag{12}$$

Within the CS-DSG3 (Cell Smoothed – Discrete Shear Gap) formulation the element domain is divided into three DSG3 sub-triangles by connecting the centroid O of the triangle with the three element nodes. In each sub-triangle the DSG formulation is used to obtain the strain-displacement matrices of the sub-triangles. Afterwards, in order to smooth the strains in the sub-triangles, the strain smoothing technique is applied over the whole triangular element. The displacement vector of the central point is assumed as an average value of the nodal displacement vectors:

$$\{d_0'\} = \frac{1}{3}\left(\begin{Bmatrix} u_1' \\ v_1' \\ w_1' \\ \theta_{1,x'} \\ \theta_{1,y'} \\ \theta_{1,z'} \end{Bmatrix} + \begin{Bmatrix} u_2' \\ v_2' \\ w_2' \\ \theta_{2,x'} \\ \theta_{2,y'} \\ \theta_{3,z'} \end{Bmatrix} + \begin{Bmatrix} u_3' \\ v_3' \\ w_3' \\ \theta_{3,x'} \\ \theta_{3,y'} \\ \theta_{3,z'} \end{Bmatrix} \right) = \frac{1}{3}\left(\{d_1'\} + \{d_2'\} + \{d_3'\}\right) \tag{13}$$

The displacement vectors corresponding to the sub-triangles read:

$$\begin{aligned} \{d'_{\Delta 1}\} &= \left(\{d_0'\} \quad \{d_1'\} \quad \{d_2'\}\right)^T \\ \{d'_{\Delta 2}\} &= \left(\{d_0'\} \quad \{d_2'\} \quad \{d_2'\}\right)^T \\ \{d'_{\Delta 3}\} &= \left(\{d_0'\} \quad \{d_3'\} \quad \{d_1'\}\right)^T \end{aligned} \tag{14}$$

The sub-triangle strain-displacement matrices can now be written and upon substituting $\{d_0'\}$ in those matrices with the values given in Eq. (13) and performing some rearrangement of the terms, the strain-displacement matrices of sub-triangles read:

$$\begin{aligned} \begin{bmatrix} [B_{mf}^{\Delta 1}] \\ -- \\ [B_s^{\Delta 1}] \end{bmatrix} &= \begin{bmatrix} \left[\frac{1}{3}[B_{mf,1}^{\Delta 1}] + [B_{mf,2}^{\Delta 1}]\right] & \left[\frac{1}{3}[B_{mf,1}^{\Delta 1}] + [B_{mf,3}^{\Delta 1}]\right] & \frac{1}{3}[B_{mf,1}^{\Delta 1}] \\ -- & -- & \\ \left[\frac{1}{3}[B_{s,1}^{\Delta 1}] + [B_{s,2}^{\Delta 1}]\right] & \left[\frac{1}{3}[B_{s,1}^{\Delta 1}] + [B_{s,3}^{\Delta 1}]\right] & \frac{1}{3}[B_{s,1}^{\Delta 1}] \end{bmatrix} \\ \begin{bmatrix} [B_{mf}^{\Delta 2}] \\ -- \\ [B_s^{\Delta 2}] \end{bmatrix} &= \begin{bmatrix} \frac{1}{3}[B_{mf,1}^{\Delta 2}] & \left[\frac{1}{3}[B_{mf,1}^{\Delta 2}] + [B_{mf,2}^{\Delta 2}]\right] & \left[\frac{1}{3}[B_{mf,1}^{\Delta 2}] + [B_{mf,3}^{\Delta 2}]\right] \\ -- & -- & \\ \frac{1}{3}[B_{s,1}^{\Delta 2}] & \left[\frac{1}{3}[B_{s,1}^{\Delta 2}] + [B_{mf,2}^{\Delta 2}]\right] & \left[\frac{1}{3}[B_{s,1}^{\Delta 2}] + [B_{s,3}^{\Delta 2}]\right] \end{bmatrix} \\ \begin{bmatrix} [B_{mf}^{\Delta 3}] \\ -- \\ [B_s^{\Delta 3}] \end{bmatrix} &= \begin{bmatrix} \left[\frac{1}{3}[B_{mf,1}^{\Delta 3}] + [B_{mf,3}^{\Delta 3}]\right] & \frac{1}{3}[B_{mf,1}^{\Delta 3}] & \left[\frac{1}{3}[B_{mf,1}^{\Delta 3}] + [B_{mf,2}^{\Delta 3}]\right] \\ -- & -- & \\ \left[\frac{1}{3}[B_{s,1}^{\Delta 3}] + [B_{s,3}^{\Delta 3}]\right] & \frac{1}{3}[B_{s,1}^{\Delta 3}] & \left[\frac{1}{3}[B_{s,1}^{\Delta 3}] + [B_{s,2}^{\Delta 3}]\right] \end{bmatrix} \end{aligned} \tag{15}$$

where $[B_{mf,i}^{\Delta j}], [B_{s,i}^{\Delta j}]$ are the nodal strain displacement matrices of the j^{th} sub-triangle's i^{th} node. The resulting smoothed strain matrices are given by:

$$\begin{bmatrix} [B_{mf*}] \\ -- \\ [B_{s*}] \end{bmatrix} = \frac{1}{3}\sum_{i=1}^{3} \begin{bmatrix} [B_{mf}^{\Delta i}] \\ -- \\ [B_{s}^{\Delta i}] \end{bmatrix} \tag{16}$$

The composite laminates constitutive matrix, well-known as the ABD matrix is defined with respect to the fiber orientation (user input). As the fiber orientation generally does not match the local x′-direction, the ABD requires an in-plane rotation thus yielding the A′ B′ D′-matrix. Finally, the mechanical stiffness matrix of the CS-DSG3 element $[K_e]$ with respect to the global coordinate system is computed using its local element counterpart $[K_e']$ and the transformation matrix [T] as follows:

$$[K_e] = [T]^T [K_e'][T] \tag{17}$$

where $[K_e']$ is computed as follows:

$$[K_e'] = A_e \left(\begin{bmatrix} [B_{mf*}] \\ -- \\ [B_{s*}] \end{bmatrix}^T \begin{bmatrix} [A'] & [B'] \\ [B'] & [D'] \end{bmatrix} \begin{bmatrix} [B_{mf*}] \\ -- \\ [B_{s*}] \end{bmatrix} \right) \tag{18}$$

2.3 Piezoelectric layer

Corresponding to the choice of mechanical displacements and electric potential as independent variables, the constitutive equations of the piezoelectric material read (Tzou, 1993):

$$\begin{aligned} \{\sigma\} &= [C^E]\{\varepsilon\} - [e]\{E\} \\ \{D\} &= [e]\{\varepsilon\} + [d^\varepsilon]\{E\} \end{aligned} \tag{19}$$

with the mechanical stress $\{\sigma\}$ in vector (Voigt) notation, the electric displacement vector $\{D\}$, the piezoelectric material Hooke's matrix $[C^E]$ at constant electric field $\{E\}$, the dielectric permittivity matrix $[d^\varepsilon]$ at constant strain $\{\varepsilon\}$, and the piezoelectric coupling matrix [e]. In the following, piezoelectric elements with electrodes on the top and bottom surfaces are considered. The piezoelectric layers are polarized in the thickness direction and their in-plane strain field is

coupled with the applied electric field across the thickness through the piezoelectric e_{31}-effect. Although the accurate modeling of the electric field in such piezopatches for bending dominated problems requires a quadratic function for the electric potential and a linear function for the electric field, a previous research has already shown that a linear approximation for the electric potential and, consequently, a constant electric field are acceptable for the present class of piezoelectric materials and typical (rather thin) geometry of piezopatches (Marinkovic et al, 2007; Marinkovic et al, 2009). Hence:

$$E = -\frac{\partial \varphi}{\partial z'} \Rightarrow E_k = -\frac{\Delta \Phi_k}{h_k} \tag{20}$$

where φ is the electric potential function across the thickness of the piezolayer, $\Delta\Phi_k$ is the difference of the electric potentials between the electrodes of the layer and h_k is the thickness of the piezolayer. Obviously, the electric field is treated layer-wisely. Equation (20) leads to a diagonal electric field – electric potential matrix $[B_\phi]$, with $1/h_k$ as a typical main diagonal element.

3 FINITE ELEMENT EQUATIONS

The focus in this paper is on static cases. The FEM equations can be obtained by using the variational principle (Kim and Lee, 1988). Performing the discretization of the structure and applying the variational formalism, one comes up with the following form of the finite element equations in linear analysis:

$$[K_{uu}]\{u\} + [K_{u\varphi}]\{\varphi\} = \{F\} \tag{21}$$

$$[K_{\varphi u}]\{u\} + [K_{\varphi\varphi}]\{\varphi\} = \{Q\} \tag{22}$$

where $[K_{uu}]$ is the mechanical stiffness matrix, $[K_{u\phi}]$ and $[K_{\phi u}]$ ($[K_{u\phi}]=[K_{\phi u}]^T$) are the piezoelectric direct and inverse coupling matrices, respectively, $[K_{\phi\phi}]$ is the dielectric stiffness matrix, vectors $\{\phi\}$and $\{u\}$ comprise the mechanical and electrical (differences of electric

potentials) degrees of freedom, respectively, while the vectors {F} and {Q} are the mechanical and electric loads, respectively. Nonlinear FEM analysis is performed incrementally and the equations read:

$$ {}^{t}\left[K_{uu}\right]{}^{t}\{\Delta u\} + {}^{t}\left[K_{u\varphi}\right]{}^{t}\{\Delta\varphi\} = {}^{t+\Delta t}\{F_{ext}\} - {}^{t}\{F_{int}\} \tag{23} $$

$$ {}^{t}\left[K_{\varphi u}\right]{}^{t}\{\Delta u\} + {}^{t}\left[K_{\varphi\varphi}\right]{}^{t}\{\Delta\varphi\} = {}^{t+\Delta t}\{Q_{ext}\} - {}^{t}\{Q_{int}\} \tag{24} $$

where the left superscript denotes at what moment in time a quantity is taken, Δ denotes the increment of a quantity, ‘ext’ and ‘int’ in the right subscript are used with quantities on the right-hand side of the equations to denote external and internal (mechanical and electric) loads, respectively.

The system matrices in Eqs. (21-24) are assembled from element matrices. The element mechanical stiffness matrix is already given in Eq. (19). The element piezoelectric coupling and dielectric stiffness matrices are computed as follows:

$$ \left[K_{u\varphi}\right] = \int_{V} \left(\begin{bmatrix} [B_{mf*}] \\ -- \\ [B_{s*}] \end{bmatrix}^{T} [e][B_{\varphi}] \right) dV \tag{25} $$

and

$$ \left[K_{\varphi\varphi}\right] = -\int_{V} \left[B_{\varphi}\right]^{T} \left[d^{\varepsilon}\right] \left[B_{\varphi}\right] dV \tag{26} $$

In this paper the cases are studied that involve either only actuation or only sensing, i.e. no mixture of those. In the actuator case, electric voltages are predefined and the structural deformation is computed. Only the first equation from the systems of equations Eqs. (21-22) (linear case) or Eqs. (23-24) (nonlinear case) is needed for the computation, whereby the mechanical loads induced through piezoelectric coupling are given as:

$$ \{F_{piezo}\} = \left[K_{u\varphi}\right]\{\varphi_{a}\} \tag{27} $$

and the computation proceeds as purely mechanical FEM computation with the external loads equal to the loads defined by Eq. (25).

In the sensor case, the excitation is mechanical in form of either mechanical forces or predefined displacements, while the electric charges are set to zero. If the structure is excited by forces, then the system of equations (Eqs. (21-22) or Eqs. (23-24)) remains fully coupled. In case of predefined displacements, the sensor voltages can be directly obtained from the second equation in Eqs. (21-22) or Eqs. (23-24):

$$\{\varphi_s\} = -\left[K_{\varphi\varphi}\right]^{-1}\left[K_{e\varphi u}\right]\{u\} \tag{28}$$

4 CO-ROTATIONAL FORMULATION

As already emphasized, the considered thin-walled structures are susceptible to large local rotations with still small strains induced. Such deformational behavior can be efficiently treated by means of a co-rotational (CR) FEM formulation. The essence of the CR-formulation consists in introduction of a local element reference frame, [E], that is attached to the material and performs the same rigid-body motion as the structural material (Fig. 2). In this manner, the overall motion can be decomposed into the rigid-body motion and purely deformational motion. Generally speaking, over the course of deformation, the rigid-body rotation differs for different points of a deformable body. However, in the present formulation, a curved shell structure is approximated by a number of linear triangular (facet) elements. Consequently, the rigid-body rotation is constant for the entire element and represented by a single rotational matrix. The strains are assumed to be small so that the deformational behavior with respect to the element reference frame, which follows the element in its rigid-body rotation, can be described as linear.

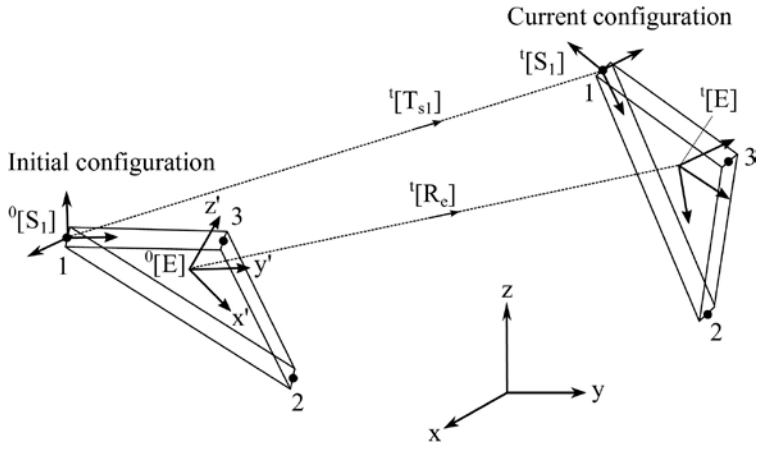

Fig. 2 Co-rotational approach

The element rotational matrix, $[R_e]$, is determined by the polar decomposition of the deformation gradient matrix, which is also constant over the element area. Once the rotational matrix is determined, the element stiffness matrix is updated as follows:

$$ {}^t[K_e] = {}^t[R_e]\,{}^0[K_e]\,{}^t[R_e]^T \tag{29} $$

The nodal rotation-free translations ${}^t\{u^r_{T,i}\}$ are then calculated by:

$$ {}^t\{u^r_{T,i}\} = \begin{Bmatrix} {}^t u^r_i \\ {}^t v^r_i \\ {}^t w^r_i \end{Bmatrix} = {}^t[R_e]^T \begin{Bmatrix} {}^t x_i \\ {}^t y_i \\ {}^t z_i \end{Bmatrix} - \begin{Bmatrix} x_i \\ y_i \\ z_i \end{Bmatrix} \tag{30} $$

In order to handle the nodal rotations, each element node is assigned a coordinate system $[S_i]$, i=1,2,3, which is initially parallel to the global system. Those nodal coordinate systems rotate as defined by the computed nodal rotations from their initial orientation $^0[S_i]$ to their current orientation $^t[S_i]$ (i=1,2,3; Fig. 2). The coordinate systems $^t[S_i]$ are updated by means of the transformation matrix $^t[T_{si}]$:

$$ {}^t[T_{si}] = {}^t[\Delta T_{si}]\,{}^{t-\Delta t}[T_{si}] \tag{31} $$

where $^t[\Delta T_{si}]$ is determined by means of the incremental nodal rotations as follows:

$$ {}^{t}\left[\Delta T_{si}\right] = \left[I\right] + \frac{\sin {}^{t}\omega}{{}^{t}\omega}\left[Spin\right] + \frac{1}{2}\left(\frac{\sin({}^{t}\omega/2)}{{}^{t}\omega/2}\right)^{2}\left[Spin\right]^{2} \tag{32} $$

with:

$$ {}^{t}\omega = \sqrt{{}^{t}\Delta\theta_{x,i}^{2} + {}^{t}\Delta\theta_{y,i}^{2} + {}^{t}\Delta\theta_{z,i}^{2}} \tag{33} $$

and:

$$ {}^{t}\left[Spin\right] = \begin{bmatrix} 0 & -{}^{t}\Delta\theta_{z,i} & {}^{t}\Delta\theta_{y,i} \\ {}^{t}\Delta\theta_{z,i} & 0 & -{}^{t}\Delta\theta_{x,i} \\ -{}^{t}\Delta\theta_{y,i} & -{}^{t}\Delta\theta_{x,i} & 0 \end{bmatrix} \tag{34} $$

Afterwards the rotational matrix ${}^{t}[R_e]$ is used to obtain the transformation matrix ${}^{t}[T_{sr,i}]$:

$$ {}^{t}\left[T_{sr,i}\right] = {}^{t}\left[R_{e}\right]{}^{t}\left[T_{si}\right] \tag{35} $$

Finally, the nodal rotations for the current configuration freed from the rigid-body motion and expressed in the global coordinate system, ${}^{t}\{\theta_{i}^{r}\}$, are equal to following components of the ${}^{t}[T_{sr,i}]$ matrix:

$$ {}^{t}\{\theta_{i}^{r}\} = \begin{Bmatrix} {}^{t}\theta_{x,i}^{r} \\ {}^{t}\theta_{y,i}^{r} \\ {}^{t}\theta_{z,i}^{r} \end{Bmatrix} = \begin{Bmatrix} {}^{t}T_{sr,i}(2,3) \\ -{}^{t}T_{sr,i}(1,3) \\ -{}^{t}T_{sr,i}(2,1) \end{Bmatrix} \tag{36} $$

Finally, by means of translations and rotations freed from rigid-body rotation, the internal forces and moments can be determined, which together with the updated stiffness matrix allows to proceed with the geometrically nonlinear FEM computations. In the actuator case, the mechanical loads induced by piezoelectric coupling (Eq. (27)) need to be rotated through ${}^{t}[R]$, whereas in the sensor case the rotation-free displacements are to be used in Eq. (28)

5 NUMERICAL EXAMPLES

The following examples consider composite structures with different types of layers. Table 1 displays the properties of all materials used in the examples, with Y denoting the Young's modulus and ν the Poisson's ratio, with indices referring to material directions. Isotropic materials and materials that are considered to be isotropic (even if they are not in reality) are described by only two parameters, Y and ν, while the omitted constants (empty cells in Table 1) are considered to be equal to zero in the examples. The stacking sequence of laminates and thickness of layers vary in the studied examples and will be specified separately.

Table 1 Material properties of the layers in the principal material directions

	T300/976	Aluminum	PTZ-4	PVDF	PIC 151	PTZ-G1195
Elastic properties						
Y_{11} [GPa]	150.0	70.3	81.3	2	61.3	63.0
Y_{22} [GPa]	9.0	-	81.3	-	61.3	63.0
Y_{33} [GPa]	9.0	-	64.5	-	48.4	63.0
υ_{12} [-]	0.3	0.345	0.33	0.29		0.3
υ_{13} [-]	0.3	-	0.43	-		0.3
υ_{23} [-]	0.3	-	0.43	-		0.3
Piezoelectric constants						
$e_{31} = e_{32}$ [Cm^{-2}]			-14.8	0.046	9.6E-6	22.86
Dielectric constant [F m^{-1}]						
d_{31} ($\times 10^{-8}$)			1.1505	0.01062	1.710	0.0254

5.1 Active Beam Structure (actuator case)

A clamped beam with a pair of collocated piezopatches bonded onto its outer surfaces is considered in this example. The geometry of the beam is given in Fig. 3. The beam is made of aluminum as carrying/passive material, while the piezopatches are made of the piezoceramic PIC 151 (Table 1). The piezopatches are polarized in opposite directions and each of them is subjected to a constant voltage of 100 V. Such a system of collocated piezopatches with opposite polarization and their symmetric position across the thickness is quite often used for actuator applications in thin-walled structures as it improves the actuation. In such a system, the piezoelectric effect tends to stretch one of the patches and contract the other one. Since the

patches are bonded to the beam, stresses are induced resulting in bending of the beam. Using the presented shell element to discretize the structure, the FE mesh with 180 elements is found to yield the converged solution. The resulting transverse displacement along the centerline is given in Fig. 4. The absolute value of the calculated tip deflection (point A, see Fig 3) is 6.07×10^{-4} m. Nestorovic et al. (2013) reported the value of 6.06×10^{-4} m for the tip deflection, by using a 9-node full-biquadratic shell element. The two results are obviously in a very good agreement.

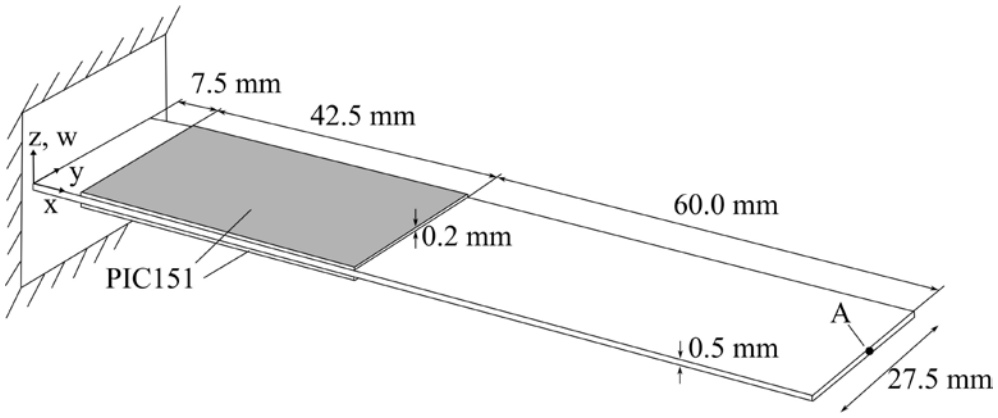

Fig. 3 Geometry of the active beam structure

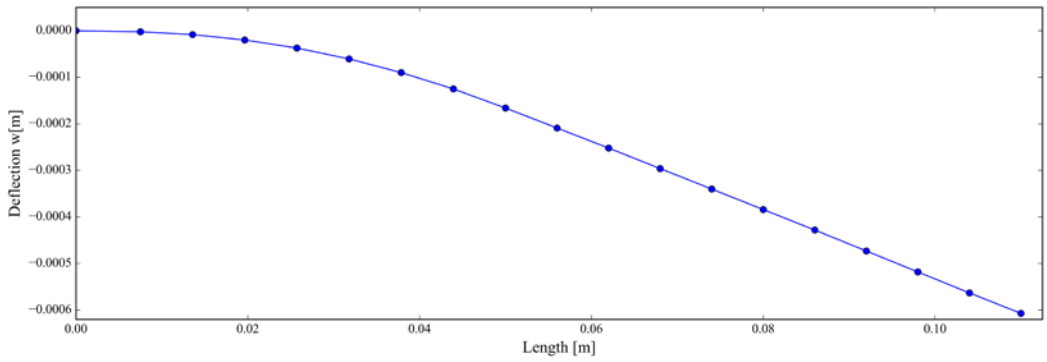

Fig. 4 Static deflection of the active beam structure at the centerline

5.2 Semi-Circular Cylindrical Composite Shell (sensor case)

This example was originally proposed by Saravanos (1997) and additionally studied by Balamurugan and Narayanan (2008). The geometry of the semi-circular cylindrical shell is presented in Fig. 5. The stacking sequence of composite is $[p/0/90/+45/-45]_{sym}$ with composite

layers made of graphite epoxy (Table 1), while the piezolayers made of PZT-4 (Table 1) are bonded to the inner and outer surface of the composite shell. The sequence is given with respect to the global x-axis. The thickness of each composite ply is 1.2×10^{-3} m and the thickness of each piezoelectric layer 2.4×10^{-3} m. The total thickness of the shell is therewith 0.0144 m. The radius R of the mid-surface is 0.1 m and the width b is 62.8×10^{-3} m. A line load F_{line} = 159.2 N/m acting in the x-direction is applied at the structure's free end. The other end is clamped. Upon the convergence analysis, the results obtained with 120 elements are taken as representative. The deformation induced by the mechanical load gives rise to electric voltages in the pezoelectic layers. Since the deformation is not the same in the two piezolayers, the induced voltages differ. For the sake of direct comparability of the obtained results with those by Saravanos (1997) and Balamurugan and Narayanan (2008), the sensor potential of the outer piezolayer is normalized in the same way proposed by the aforementioned authors, i.e. by ($\varphi_s\times122\times10^{-10}$/h).

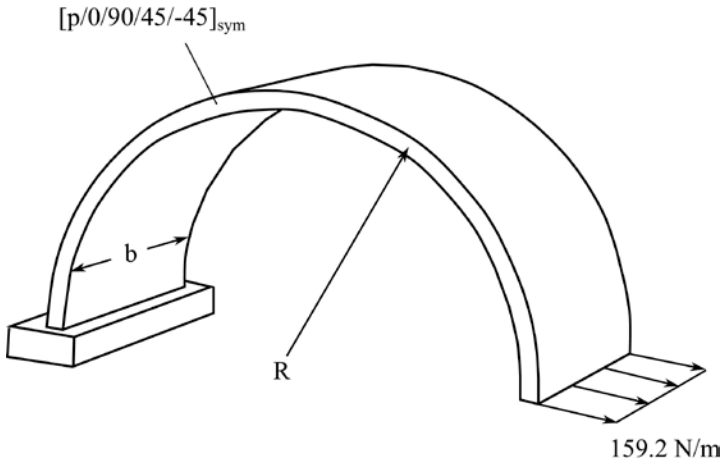

Fig. 5 Semi-circular cylindrical composite cantilevered shell with PZT sensor/actuator at the top and bottom surfaces

Whereas Saravanos (1997) gives a theoretical result for an infinite number of sensors, each across the structure's width and with an infinitesimal length along the hoop-distance, Balamurugan and Narayanan (2008) give a result for a more realistic case of 15 sensors along the hoop. The results by present element are also computed for 15 sensors along the hoop and are very similar to those by Balamurugan and Narayanan (2008). The three results depicted in Fig. 6

demand a comment. Obviously, the result by Saravanos (1997) shows different principle tendency compared to the other two results – it is not symmetric with respect to the mid-value of the normalized hoop distance (0.5) and, additionally, the value at the free end is not zero. At this point it should be emphasized that the theoretical result for an infinite number of sensors across the hoop with both the present element and element by Balamurugan and Narayanan (2008) would be zero at the free end. This is due to the fact that both the bending moment and in-plane force are zero at the free end, and if the sensor voltages are only a result of the piezoelectric e_{31}-effect, then the induced voltage is zero at that point. Also, considering the cross-sectional loads along the hoop-distance, the induced sensor voltage must be symmetric if, again, only the piezoelectric e_{31}-effect is accounted for. Both aspects, i.e. non-symmetry and non-zero value at the free end, suggest that the formulation by Saravanos (1997) accounts not only for the e_{31}-effect but also for the piezoelectric coupling involving transverse shear strains. Hence, the result by the present element is actually directly comparable only with the results by Balamurugan and Narayanan (2008). But even in that comparison, the difference in results call for a comment. It may be seen that the results by Balamurugan and Narayanan yield somewhat smaller values compared to the results by present element. This may be attributed to the fact that Balamurugan and Narayanan account for quadratic distribution of the electric potential across the thickness of piezolayers, which leads to stiffer structural behavior (Marinković et al., 2007) and therewith to lower values for sensor voltages. Actually, Balamurugan and Narayanan use the same argument to explain the difference between their result and that by Saravanos, but in the authors' opinion, this argument is at least incomplete as it neglects the non-symmetry of the Saravanos' result.

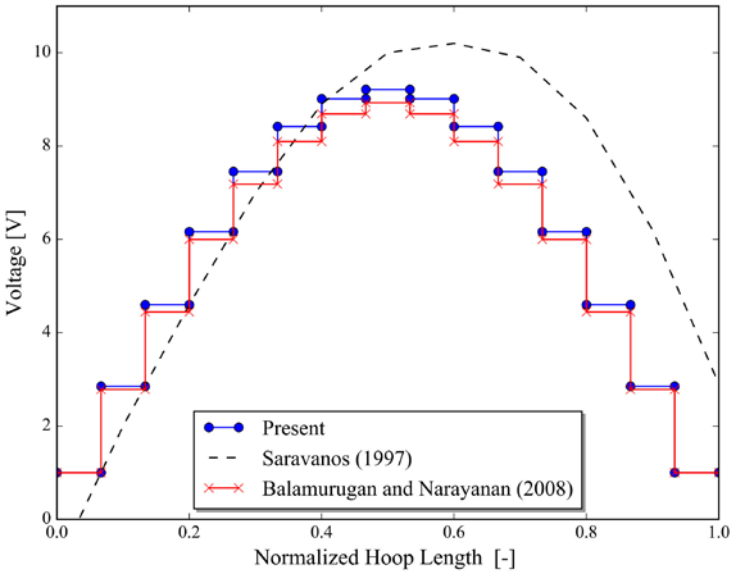

Fig. 6 Semi-circular cylindrical composite shell - voltage distribution of the outer piezolayer

5.3 Piezoelectric composite plate (nonlinear actuator case)

In the following example a laminated piezoelectric square plate, with an edge length a = 0.4 m, exposed to piezoelectric excitation is studied. The structure is made of three layers, the outer two are made of PZT-G1195N and have a thickness of 0.2 mm and the mid-layer is a T300/976 layer with a thickness of 0.15 mm and fiber orientation of 90° with respect to the x-axis. The piezolayers are subjected to an input voltage of 300 V, thus providing a large enough excitation that leads to visible nonlinear effects in the response of the plate. Two different boundary conditions are considered: a clamped plate and a simply supported plate (see Fig 7, case I, II). In order to capture the curved geometry upon deformation adequately, an FE mesh with 128 elements was used.

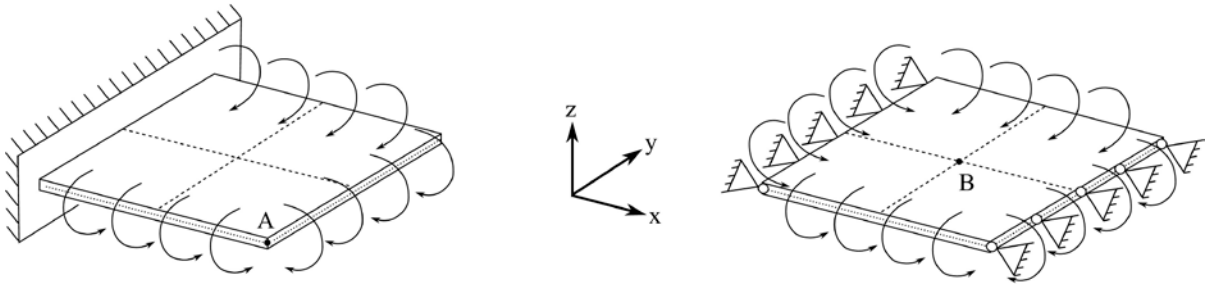

Fig 7 Initial geometry and boundary conditions of the cases I (left) and II (right)

Both cases have already been considered by Marinković et al. (2008) using the updated Lagrangian formulation and a degenerated 9-node shell element. Points A and B are chosen as representative to follow their displacements with the increasing load. The load-displacement diagrams for points A and B are given in Fig. 8 while Table 2 summarizes the displacements for the full load for linear and geometrically nonlinear FEM computation. The results obtained by the current formulation are in a very good agreement with those by Marinković et al. (2008). The differences in case I are less than 0.1% and in case II less than 0.8% in both linear and geometrically nonlinear static analyses. Obviously, the geometrically nonlinear effects are much less pronounced in case I as they are only the consequence of the geometry change during the deformation, which however does not influence the stiffness dramatically because the deformation remains bending dominated with no or negligible membrane effects. Oppositely, in case II, as soon as the deformation is initiated, significant membrane effects arise and the structure behaves stiffer. Hence, in the initial configuration it is the bending stiffness that plays the major role, but over the course of deformation the membrane stiffness takes over the primary role. This leads to notable differences between the linear and geometrically nonlinear results, as seen in Fig. 8 right.

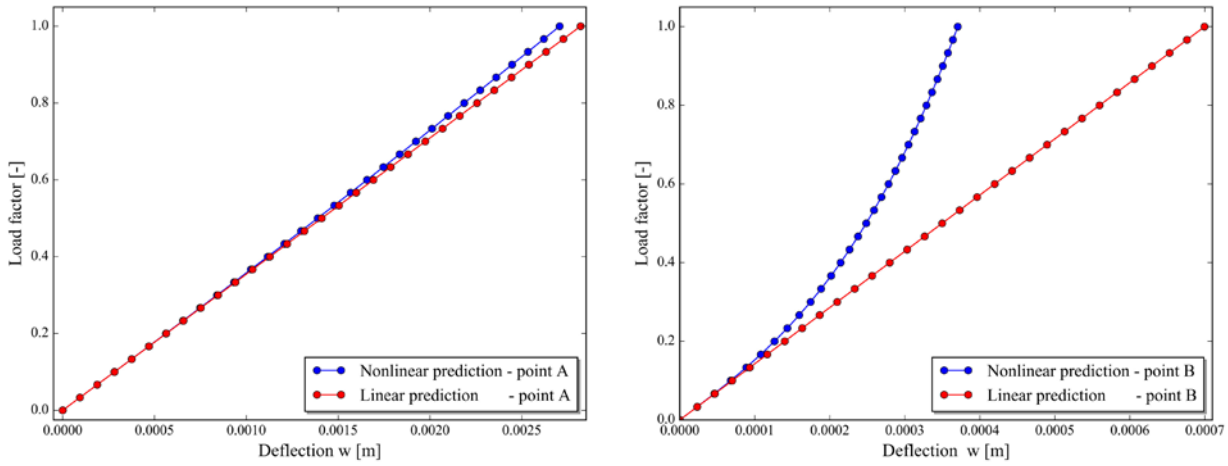

Fig. 8 Linear and nonlinear deflections at representative points: A (case I, left) and B (case II, right)

Table 2 Representative points deflections – linear and nonlinear results

Linear static	Present	Marinković et al. (2008)
Case A – w_A [m] ($\times 10^{-3}$)	2.820	2.8
Case B – w_B [m] ($\times 10^{-3}$)	0.699	0.7
Nonlinear static		
Case A – w_A [m] ($\times 10^{-3}$)	2.705	2.7
Case B – w_B [m] ($\times 10^{-3}$)	0.371	0.37

5.4 Piezoelectric Bimorph Beam - static analysis

The piezoelectric bimorph pointer consists of two uniaxial piezoelectric layers with opposite polarization. The example is well-documented in the literature and has been practically an inevitable benchmark example for a number of similar developments, e.g., Hwang and Park (1993), Chee et al. (1997), Nguyen-Thoi et al. (2013), etc. The geometry of the bimorph beam is depicted in Fig. 9. The length L of the beam is 0.1 m, the total height H is 0.1 mm and the width W is 5 mm. The beam layers are made of uniaxial PVDF polarized in the thickness direction. It should be noted that PVDF is a rather compliant material and the contribution of the structure's dead weight onto the observed deflection is probably non-negligible. This effect is, however, neglected here, which only deepens its academic nature.

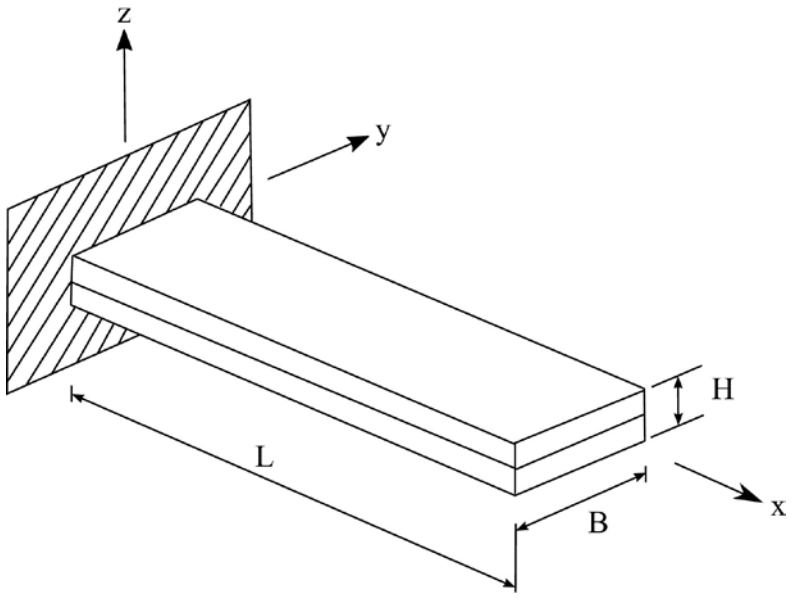

Fig. 9 Piezoelectric bimorph beam geometry

In the following, the bimorph beam is considered as actuator and sensor. For the actuator case only the result of the linear analysis is presented, whereas the sensor case has been treated both linearly and geometrically nonlinearly. Because of the geometrically nonlinear analysis, the mesh with 40 elements is chosen.

First the bimorph beam is considered as an actuator. Hence, the voltage of $\Delta\varphi = 1\text{V}$ is applied over its thickness and along the entire length. It is a straightforward exercise to analytically derive the result based on the Euler-Bernoulli beam theory and the constitutive equations of linear piezoelectricity, which leads to a quadratic function for the beam deflection:

$$w(x) = \frac{3}{2}\frac{e_{31}}{YH^2}\Delta\varphi\, x^2 \tag{37}$$

Eq. (37) yields the tip (x=0.1 m) deflection of 3.45×10^{-7} m, which is also the result yielded by the FE model using the present element. The deflection of the whole beam computed by the FE model is shown in Fig. 10.

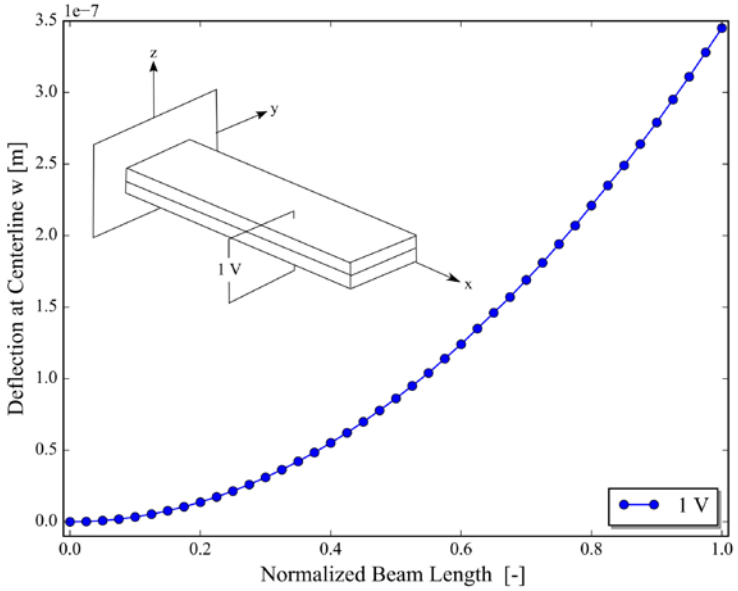

Fig. 10 Static deflection of bimorph beam subjected with input voltage of 1V

The bimorph beam is next studied as a sensor case. Deformation caused by external loads results in electric charges due to the direct piezoelectric effect and therewith an electric voltage is

induced between the electrodes on the outer surfaces. A tip deflection of 0.01 m is imposed as a boundary condition (see Fig. 11) which leads to a linear distribution of the bending moment along the length. The obtained distribution of the electric voltage along the length of the beam is directly affected by the number and distribution of the pairs of sensor electrodes. Each pair of sensor electrodes yields a value of the electric voltage averaging the strain over the part of the structure covered by the sensor. In such a case, it is expected that the electric voltage increases gradually in equal increments along the beam length for equally long sensors, which finally results in a staircase function. The step stair voltage distribution is verified by considering the structure as consisting of 6 and 20 sensors. The adequate sensor voltage distribution is easily recognized in Fig 11.

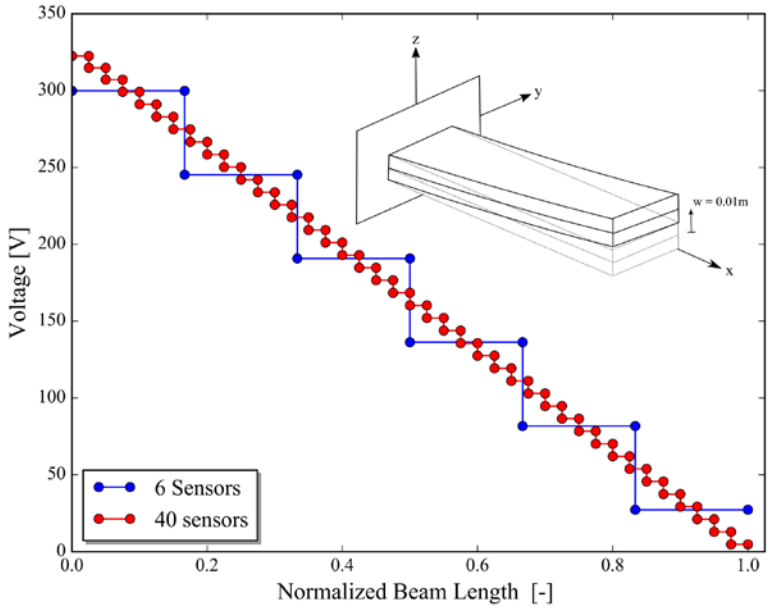

Fig. 11 Electric voltage distribution of the bimorph beam with an imposed tip deflection of 0.01 m

The sensor case is also considered as geometrically nonlinear. For this purpose, the beam is exposed to the tip load of 0.2 N. Sensor 1 for the case with 20 sensors, which is at the clamped end of the beam, is taken as representative to show the development of the induced voltage with the increasing load. This result is given in Fig. 12. As the deformation proceeds, the membrane effects in the structure gain on importance and the structure behaves stiffer compared to the

behavior predicted by the linear analysis. Additionally, as the beam bends, the beam tip moves also along the length direction (x-direction) towards the clamped end, so that the reaction moment at the clamp becomes smaller. This is reflected in the computed sensor voltage that is obviously smaller than predicted by the linear analysis.

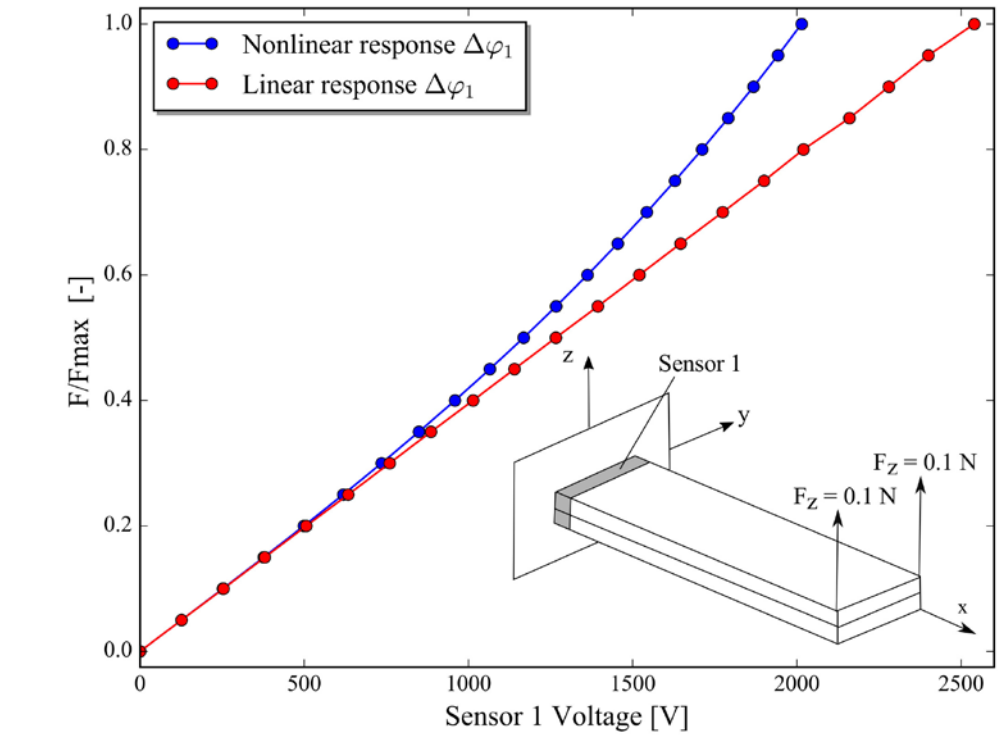

Fig. 12 Load voltage diagram of beam tip subjected with a tip load of 0.2 N

Fig. 13 shows the voltage distribution along the length of the beam computed in linear and geometrically nonlinear analysis for $F=F_{max}$. One may notice that the increase of electric voltage between consecutive sensors is not constant any more, but it becomes larger toward the clamped end. This is due to the fact that the cross-sectional in-plane forces (in length direction) are larger for the sensors closer to the free end of the beam in the deformed configuration. Since bending stiffness is smaller than the membrane stiffness, force acting as a transverse force will typically induce larger sensor voltages as a consequence of bending compared to the case in which the same force acts in-plane thus inducing sensor voltage through membrane deformation.

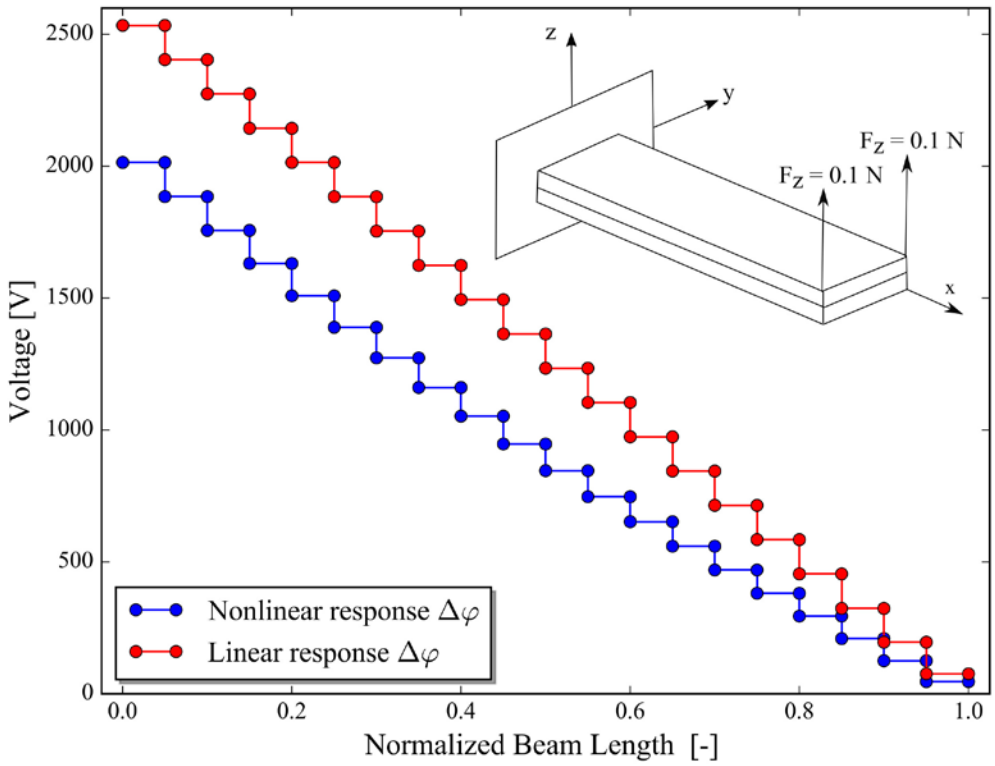

Fig. 13 Electric voltage distribution of the Bimorph Beam subjected with tip load of 0.2 N

5.5 Shape control of piezoelectric composite plate

This example was originally proposed by Kioua and Mirza (2000) and is also studied by a number of authors (e.g. Marinković, 2007). It addresses the possibility of static shape control of shell structures by means of piezoelectric actuation. A simply supported square plate (0.254×0.254 m) made of fiber reinforced composite material with bonded piezoelectric layers is considered. The stacking sequence of the composite plate is $[p/0/90/0]_{sym}$. The total thickness of the plate is 1.336 mm. The passive layers have the same thickness of 0.138 mm and are made of T300/976. The piezoelectric composite layers have a thickness of 0.254 mm and are made of PZT G1195N. A FE mesh with 200 elements yields representative results.

The surface of the plate is initially subjected to uniformly distributed pressure of 200 N/m². Furthermore, a constant voltage is applied to the oppositely polarized piezolayers, thus inducing

bending moments uniformly distributed over the shell edges. The actuator voltage is increased starting from 0 V until the shape is found that mostly corresponds to the initial/undeformed shape of the structure. The solution of Kioua and Mirza (2000) is based on the Ritz analysis and it yields a flat shape for the voltage of 27 V (Fig. 14). Clearly, a combination of surface pressure and bending moments uniformly distributed over the outer edges of a simply supported plate cannot result in a shape that is identical to the initial one. However, Kioua and Mirza (2000) obtained such a solution as a consequence of deficiency of the shape functions they used in their work. They used polynomials, the degree of which goes up to two (quadratic), whereas the actual solution requires polynomials of at least fourth degree for this specific case. The diagram in Fig. 14 depicts the FE solution by the present element together with the Ritz solution by Kioua and Mirza (2000). Compared to the FEM solution reported by Marinković et al. (2007), the present FEM results show rather small differences as obvious from Table 3.

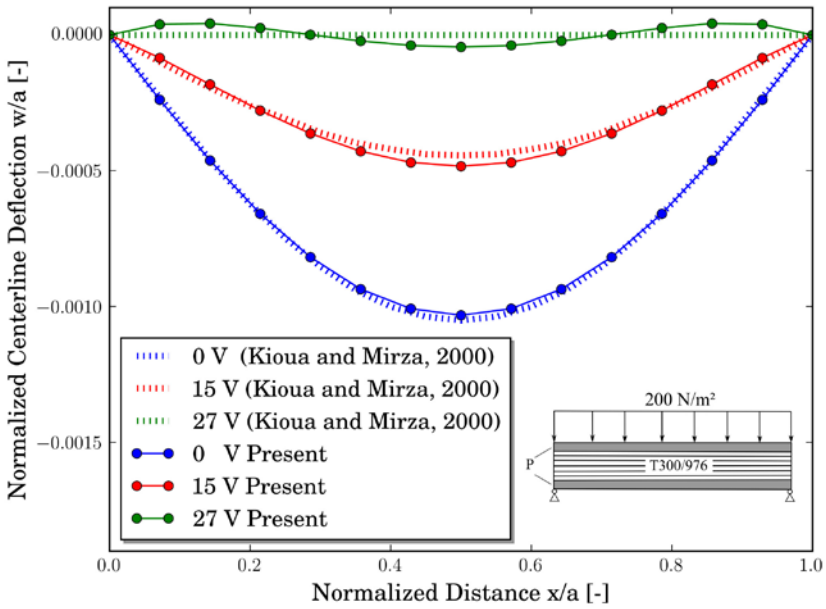

Fig. 14 Shape control of a simply supported composite plate

Table 3 Results Shape control of piezoelectric composite plate

Center node deflection [m] ($\times 10^{-3}$)	Present	Kioua and Mirza (2000)	Marinković (2007).
Applied voltage 0 V	-0.045	0.000	-0.048
Applied voltage 15 V	-0.484	-0.439-	-0.487
Applied voltage 27 V	-1.032	-1.051	-1.049

6 CONCLUSIONS

Composite laminates with piezoelectric layers that may take the sensor or actuator role open a wide range of possibilities for actively controlled structural behavior. It involves mechanical and electric fields as well as their coupling. Highly efficient, reliable and accurate tools are required in order to check various design solutions and control strategies.

The linear 3-node shell element is proposed in this paper as a reply to this demand. It covers modeling of composite laminates with directionally dependent material properties including piezoelectric layers that couple the in-plane strains to the electric field that acts across the thickness. High meshing ability of triangles clearly belongs to advantages of this element. But this advantage is inevitably accompanied with the drawback of stiffer modeled behavior, thus calling for somewhat finer meshes. The ‘descrete shear gap’ concept together with the strain smoothing technique was additionally applied to address the problem of stiff models and locking effects.

A very important aspect of the paper is the extension of formulation to geometrically nonlinear analysis based on the co-rotational concept. The concept is very convenient for structures experiencing finite rotations with infinitesimal strains. Hence, the considered thin-walled piezoelectric laminates are a very good candidate to apply the CR-concept. The rigid-body rotation is accounted for on the element level. The aforementioned requirement for somewhat finer meshes actually talks in favor of such an approach – with a finer mesh, the local rigid-body rotation is more accurately described. All the considered examples - linear and geometrically nonlinear, actuator and sensor cases - demonstrate high agreement with the reference solutions and therewith applicability of the element and CR-formulation.

In the future work the formulation should be extended to account for other types of piezoelectric couplings. Piezoelectric fibers polarized in the length direction (in-plane polarization) would be

of special interest. In addition, since the co-rotational approach separates geometrical from material nonlinearities, it represents a solid basis to extend the formulation to materially nonlinear behavior. Particularly the nonlinearities in piezoelectric coupling at larger values of electric potential are interesting.

References

Aridogan U and Basdogan I (2015) A review of active vibration and noise suppression of plate-like structures with piezoelectric transducers. *Journal of Intelligent Material Systems and Structures* 26(12): 1455-1476.

BalamuruganV and Narayanan S (2008) A piezolaminated composite degenerated shell finite element for active control of structure with distributed piezosensors and actuators. *Smart Materials and Structures* 17(3): 1-18.

Ballhause D, D'Ottavio M, Kröplin B and Carrera E (2005) A unified formulation to assess multilayered theories for piezoelectric plates. *Computers & Structures* 83(15–16): 1217-1235.

Benjeddou A (2000) Advances in piezoelectric finite element modeling of adaptive structural elements: a survey. *Computers and Structures* 76(1-3): 347-363.

Bletzinger KU, Bischoff M and Ramm E (2000) A unified approach for shear-locking-free triangular and rectangular shell finite elements. *Computers & Structures* 75(3): 321-334.

Chee CYK, Tong L, Steven GP (1999) A mixed model for composite beams with piezoelectric actuators and sensors. *Smart Materials and Structures* 8(3): 417–432.

Chrisfield MA and Moita GF (1996) A co-rotational formulation for 2-D continua including incompatible modes. *International Journal for Numerical Methods in Engineering* 39(15): 2619-2633.

Cinefra M, Carrera E and Valvano S (2015a) Variable Kinematic Shell Elements for the Analysis of Electro-Mechanical Problems. *Mechanics of Advanced Materials and Structures* 22(1-2): 77–106.

Cinefra M, Valvano S and Carrera E (2015b) A layer-wise MITC9 finite element for the free-vibration analysis of plates with piezo-patches. *International Journal of Smart and Nano Materials* 6(2): 84–104.

Dökmeci CM (1990) Shell Theory for Vibrations in Piezoceramics Under a Bias. *IEEE Transactions on Ultrasonics, Ferroelectrics, and Frequency Control* 37(5): 369-385.

Felippa C and Haugen B (2005) A unified formulation of small-strain corotational finite elements: I. theory. *Computer Methods in Applied Mechanics and Engineering* 194: 2285–2335.

Gabbert U, Köppe H, Seeger F and Berger H (2002) Modeling of smart composite shell structures. *Journal of Theoretical and Applied Mechanics* 3(40): 575-593.

Hwang WS and Park HC (1993) Finite element modeling of piezoelectric sensors and actuators, *AIAA Journal* 31(5): 930–937.

Irons BM (1976) The semiloof shell element. Ashwell DG and Gallagher RH. (Eds.): Finite elements for thin shells and curved membranes. Chapter 11: pp. 197-222, Wiley.

Kim YH and Lee SW (1988) A Solid Element Formulation for Large Deflection Analysis of Composite Shell Structures. *Computers and Structures* 30:269–274.

Kioua H and Mirza S (2000) Piezoelectric induced bending and twisting of laminated composite shallow shells. *Smart Materials and Structures* 9(4): 476-484.

Klinkel S, Wagner W (2008) A piezoelectric solid shell element based on a mixed variational formulation for geometrically linear and nonlinear applications. *Computers and Structures* 86(1-2): 38-46.

Kulikov GM and Plotnikova SV (2011) Exact Geometry Piezoelectric Solid-Shell Element Based on the 7-Parameter Model. *Mechanics of Advanced Materials and Structures* 18(2): 133–146.

Kulkarni SA and Bajoria KM (2007) Large deformation analysis of piezolaminated smart structures using higher-order shear deformation theory. *Smart Materials and Structures* 16: 1506-1516.

Lee CK (1990) Theory of Laminated Piezoelectric Plates for the Design of Distributed Sensors/Actuators. Part I: Governing Equations and Reciprocal Relationships, *Journal of the Acoustical Society of America* 87(3): 1144-1158.

Lee CK and Moon FC (1990) Modal Sensors/Actuators *Journal of Applied Mechanics* 57(2): 434-441.

Lee S, Cho BC, Park HC, Goo NS and Yoon KJ (2004) Piezoelectric Actuator–Sensor Analysis using a Three-dimensional Assumed Strain Solid Element. *Journal of Intelligent Material Systems and Structures* 15: 329-338.

Lentzen S, Klosowski P and Schmidt R (2007) Geometrically nonlinear finite element simulation of smart piezolaminated plates and shells. *Smart Materials and Structures* 16: 2265-2274

Marinkovic D (2007) A new finite composite shell element for piezoelectric active structures. *Fortschritts-Bericht VDI* 20(406).

Marinković D and Marinković Z (2012) On FEM modeling of piezoelectric actuators and sensors for thin-walled structures. *Smart Structures and Systems* 9 (5): 411-426.

Marinković D, Köppe H and Gabbert U (2007) Accurate modeling of the electric field within piezoelectric layers for active composite structures. *Journal of Intelligent Material Systems and Structures* 18(5): 503-513.

Marinković D, Köppe H and Gabbert U (2008) Degenerated shell element for geometrically nonlinear analysis of thin-walled piezoelectric active structures. *Smart Materials and Structures* 17(1): 1-10.

Marinković D, Köppe H and Gabbert U (2009) Aspects of modeling piezoelectric active thin-walled structures. Journal of Intelligent Material Systems and Structures 20(15): 1835-1844.

Marinković, D, Köppe H and Gabbert U (2006) Numerically efficient finite element formulation for modeling active composite laminates. *Mechanics of Advanced Materials and Structures.* 13(5): 379-392.

Milazzo, A (2016) Unified formulation for a family of advanced finite elements for smart multilayered plates. *Mechanics of Advanced Materials and Structures.* 23(9): 971-980.

Nestorovic T, Shabadi S, Marinkovic D and Trajkov M (2013) Modeling of piezoelectric smart structures by implementation of a user defined shell finite element. *Facta Universitatis* 11(1): 1-12.

Nestorovic T, Shabadi S, Marinkovic D and Trajkov M (2014) User defined finite element for modeling and analysis of active piezoelectric shell structures. *Meccanica* 49(8): 1763-1774.

Nguyen V, Zehn M and Marinković D (2016) An efficient co-rotational FEM formulation using a projector matrix. *Facta Universitatis series Mechanical Engineering* 14(2): 227-240.

Nguyen-Thoi T, Phung-Van P, Thai-Hoang C and Nguyen-Xuan H (2013) A Cell-based Smoothed Discrete Shear Gap method (CS-DSG3) using triangular elements for static and free vibration analyses of shell structures. *International Journal of Mechanical Sciences* 74: 32-45.

Phung-Van P, De Lorenzis L, Thai CH, Abdel-Wahab M and Nguyen-Xuan H (2015) Analysis of laminated composite plates integrated with piezoelectric sensors and actuators using higher-order shear deformation theory and isogeometric finite elements. *Computational Materials Science*. 96(B): 495-505.

Rabinovitch O (2005) Geometrically nonlinear behavior of piezoelectric laminated plates. *Smart Materials and Structures* 14(4): 785-798.

Saravanos DA (1997) Mixed Laminate Theory and Finite Element for Smart Piezoelectric Composite Shell Structures. *AIAA Journal* 35(8): 1327-1333.

Stanak P, Tadeu A, Sladek J and Sladek V (2015) Meshless analysis of piezoelectric sensor embedded in composite floor panel. *Journal of Intelligent Material Systems and Structures* 26(15): 2092-2107.

Tzou HS (1993) Piezoelectric Shells: Distributed Sensing and Control of Continua. *Kluwer Academic Publishers*, Netherlands.

Wang BT and Rogers CA (1991) Laminate Plate Theory for Spatially Distributed Induced Strain Actuators, *Journal of Composite Materials* 25(4): 433-452.

Willberg C and Gabbert U (2012) Development of a three-dimensional piezoelectric isogeometric finite element for smart structure applications. *Acta Mechanica* 223: 1837-1850.

Zemčík R, Rolfes R, Rose M and Tessmer J (2007) High performance four node shell element with piezoelectric coupling for the analysis of smart laminated structures. *International journal for numerical methods in engineering* 70(8): 934-961.